Supporting Information

Degradation Mechanisms at the $Li_{10}GeP_2S_{12}$ / $LiCoO_2$ Cathode Interface in an All-Solid-State Lithium Ion Battery

Wenbo Zhang[a], Felix H. Richter[a,b], Sean. P. Culver[a], Thomas Leichtweiss[a], Juan G. Lozano[b], Christian Dietrich[a], Peter G. Bruce[b], Wolfgang G. Zeier[a*], Jürgen Janek[a*]

[a] Physikalisch-Chemisches Institut & Center for Materials Research, Justus-Liebig-Universität Giessen, Heinrich-Buff-Ring 17, 35392 Giessen, Germany

[b] Departments of Materials and Chemistry, University of Oxford, OX1 3PH, Oxford, United Kingdom

Email:

wolfgang.g.zeier@phys.chemie.uni-giessen.de;

juergen.janek@phys.chemie.uni-giessen.de.

The $LiNb_xTa_{1-x}O_3$ coating layer. It has been reported that an oxide coating layer can suppress unfavorable space charge layers in the SE, as well as interfacial reactions.[1,2] As such, the $LiCoO_2$ particles used in this work were coated with a thin layer of $LiNb_xTa_{1-x}O_3$, which was shown to enhance SSB performance in one of our previous papers.[3] The bare $LiCoO_2$ particles exhibit very smooth surfaces, which then appear to be covered by a thin, coarse layer after coating (Figure S1). A clear boundary separating the layered $LiCoO_2$ and the 10 nm thick, amorphous coating layer can be seen under high resolution ADF-STEM (Figure S1d). The presence of tantalum and niobium was shown by XPS (see Figure S2). Signatures with binding energies around 25 eV and 206 eV correspond well with the binding energies of tantalum 4f and niobium 3d, respectively. Thus, it is concluded that the surface of the $LiCoO_2$ particles has been successfully coated with a thin, amorphous layer of $LiNb_xTa_{1-x}O_3$.

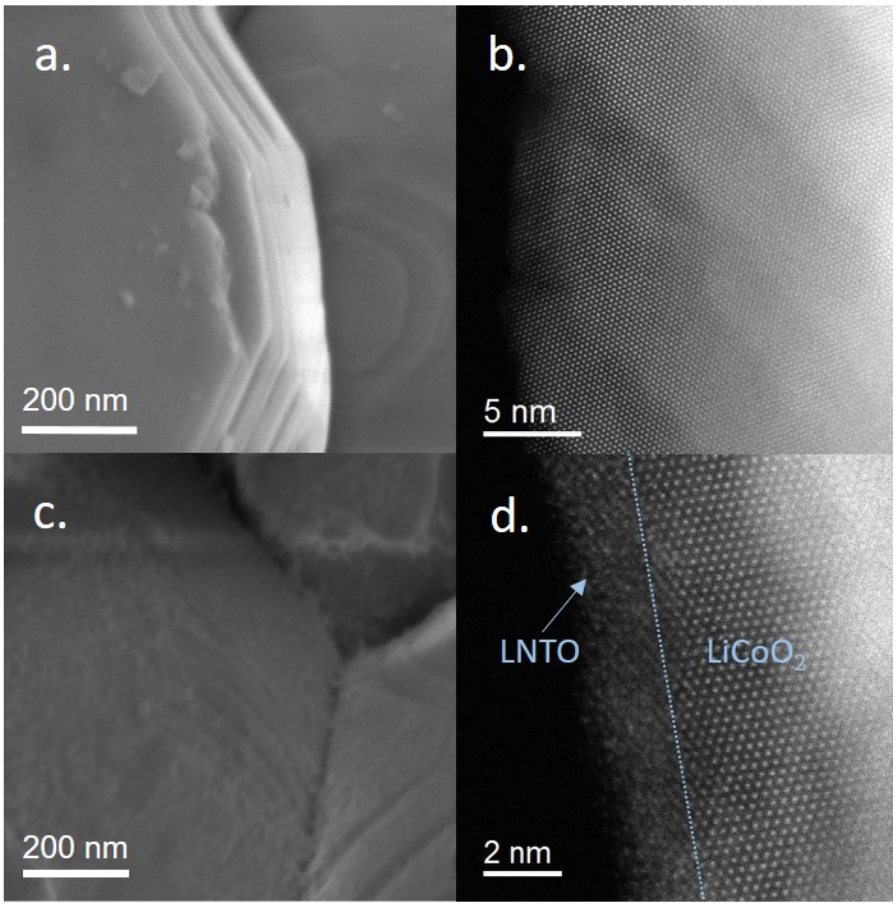

Figure S1: (a) SEM image of bare $LiCoO_2$ (b) ADF-STEM image of bare $LiCoO_2$ along the [211] direction. (c) SEM image of 1 wt% $LiNb_{0.5}Ta_{0.5}O_3$ coated $LiCoO_2$. (d) ADF-STEM images of the coated $LiCoO_2$ along the [211] direction.

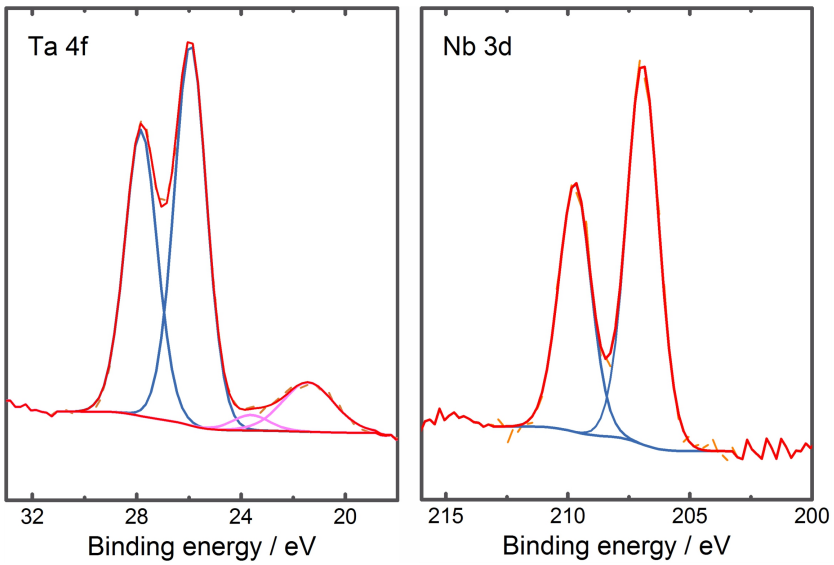

Figure S2: XPS characterization of $LiNb_xTa_{1-x}O_3$ coated $LiCoO_2$. Left: photoemission line of Ta 4f. Right: photoemission line of Nb 3d.

Combining ADF-STEM and XPS characterization, we conclude that the surface of the $LiCoO_2$ particles is coated with a thin amorphous layer of $LiNb_xTa_{1-x}O_3$.

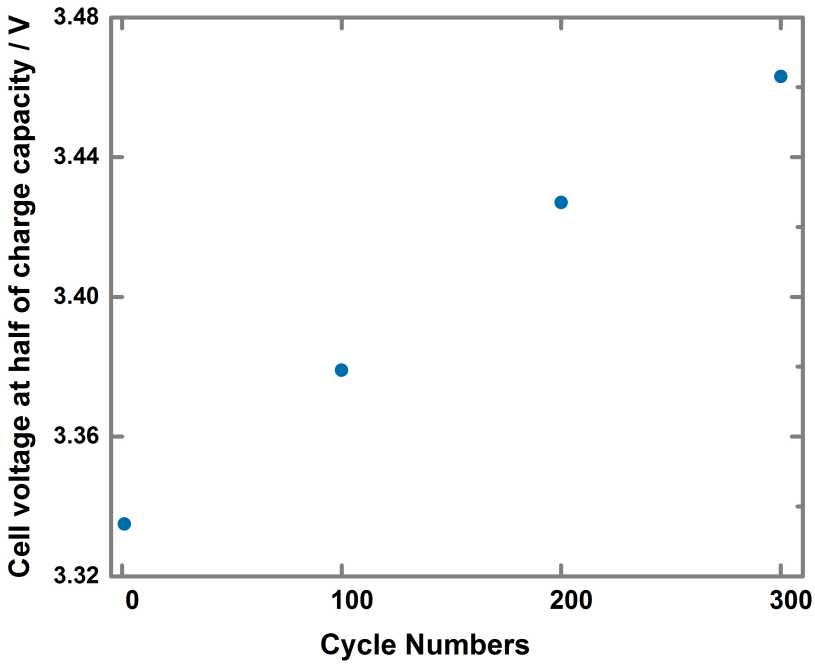

Figure S3: Comparison of cell voltages for In/LGPS/c-$LiCoO_2$ cells at SOC = 0.5 after the 1st, 100th, 200th and 300th charge. A linear increase of the cell voltage with increasing cycle numbers is observed, indicating the increase in overpotential and thus the increased internal resistance of the SSB.

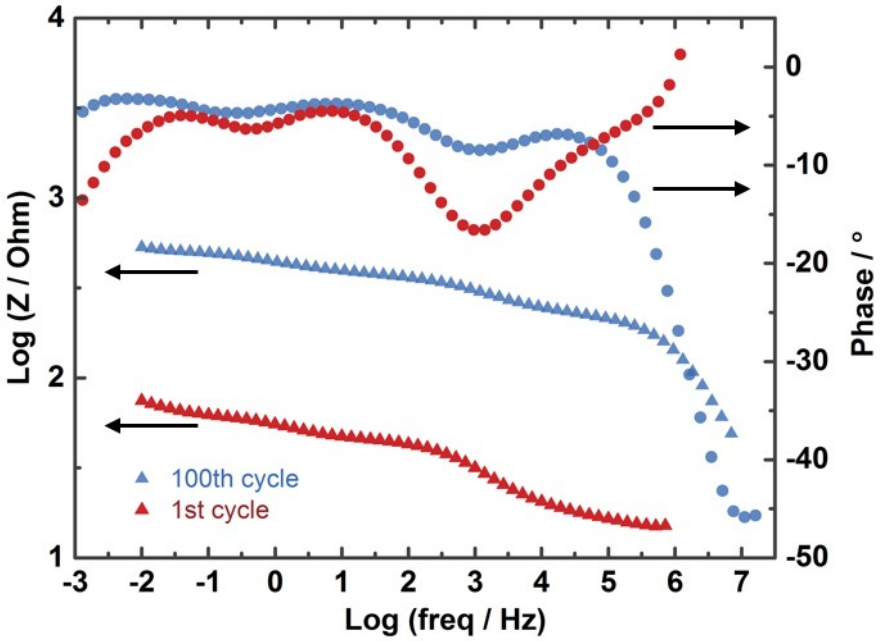

Figure S4: Bode plot of impedance spectra of SSB after 1st and 100th charge.

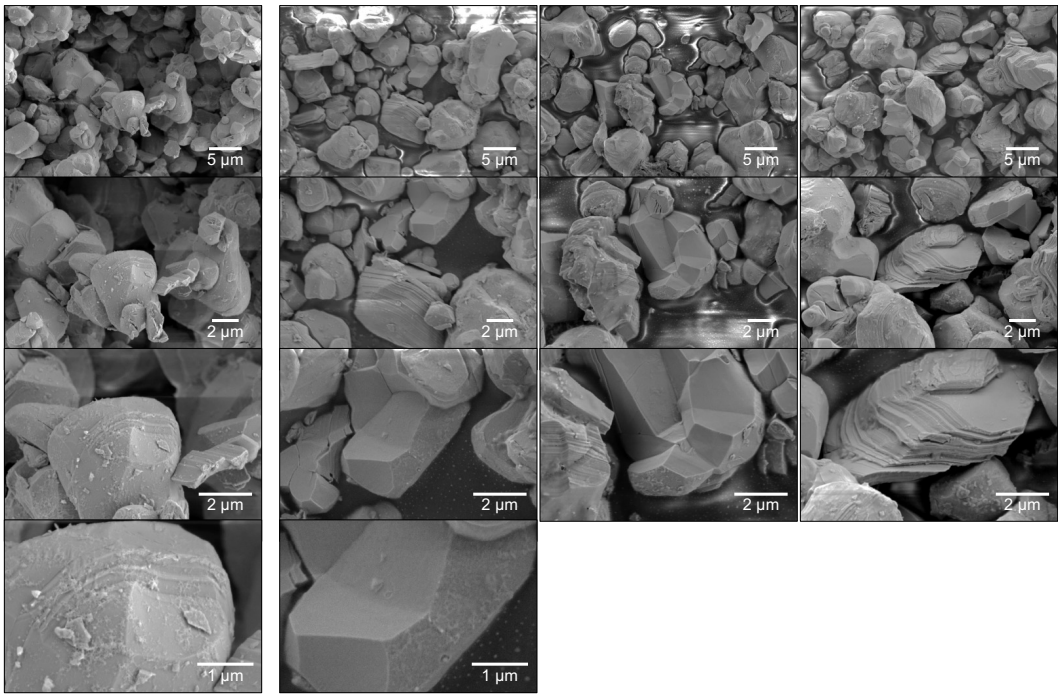

Figure S5: SEM images of pristine c-$LiCoO_2$ particles before cycling (left column) and of c-$LiCoO_2$ particles extracted from cells after 300 cycles (right columns).

Local structural observation by ADF-STEM. Figure S6 shows high resolution ADF-STEM images of the cycled $LiCoO_2$ particles. For comparison, the uncoated $LiCoO_2$ particles that failed after only 1 cycle are also provided (Figure S6 a). The structure becomes disordered, with multiple, nanometer-sized $LiCoO_2$ domains with randomly distributed orientations. The particle surface can even become amorphous at some points. Furthermore, EELS line scans on the surface of the uncoated $LiCoO_2$ reveal that the grain mismatched area contains disordered $LiCoO_2$.

In the case of c-$LiCoO_2$, no surface restructuring is observed after 110 cycles (Figure S6 b) or 300 cycles (Figure S 6c). The crystalline structure of c-$LiCoO_2$ resembles that of the pristine samples prior to the interface with the coating layer. Thus, the coating seems to be effective at preventing deleterious surface structural transformations. Further EELS analysis supporting this conclusion is presented in Figure S7.

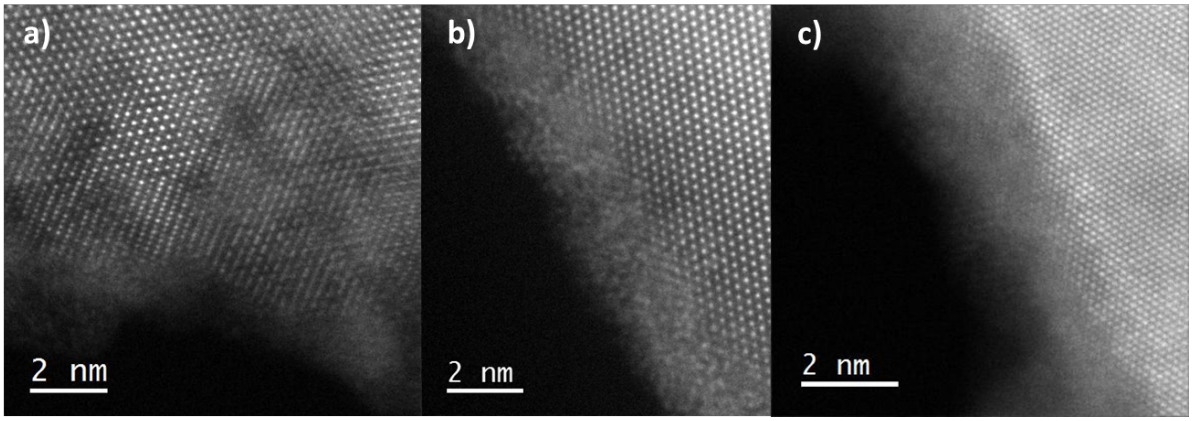

Figure S6: High-resolution ADF- STEM images of the surface of (a) bare $LiCoO_2$ after 1 cycle, (b) c-$LiCoO_2$ after 110 cycles and (c) c-$LiCoO_2$ after 300 cycles.

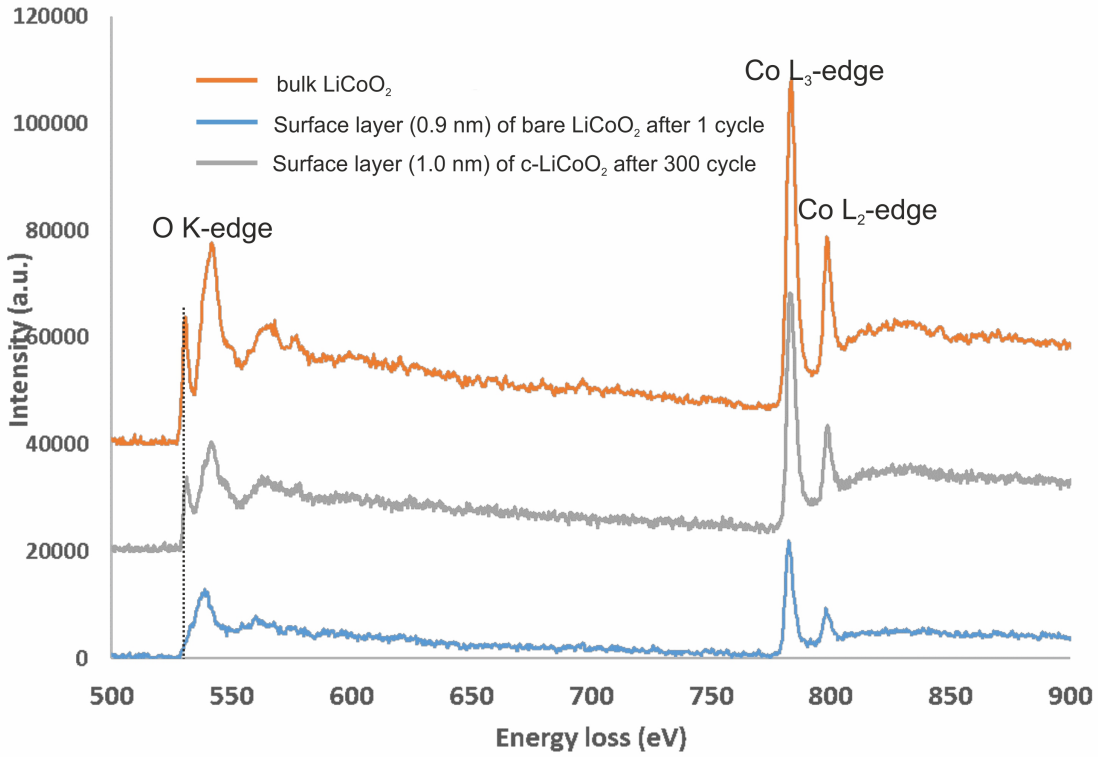

Figure S7: EELS spectra taken for the bulk of bare $LiCoO_2$, the surface of bare $LiCoO_2$ after 1 cycle and the surface of c-$LiCoO_2$ after 300 cycles. The O K-pre-edge is absent in the spectra taken at the surface of the bare $LiCoO_2$ particle after cycling, which is in good agreement with the presence of disordered $LiCoO_2$.

EELS was carried out in order to unravel more information about local chemical bonding of elements at the $LiCoO_2$ surfaces. EELS line scans of the O K-edge show, from bulk to surface, an absence of the characteristic ionization O K-pre-edge at 530 eV (Figure S7), when bare $LiCoO_2$ was investigated. Meng *et al*. reported that a disordered $LiCoO_2$ layer forms immediately, when $LiCoO_2$ is in direct contact with LiPON.[4] The O K-pre-edge of the disordered $LiCoO_2$ layer disappears once the sample is exposed to air during sample transport, while it remains intact in the ordered bulk $LiCoO_2$. Our observations appear to be quite similar. It is thus quite likely that disordered $LiCoO_2$ forms at the bare $LiCoO_2$/LGPS interface. In comparison, these changes were not observed near the coating layer/$LiCoO_2$ even after 300 cycles, indicating that the coated particles do not form disordered $LiCoO_2$ at the surface. This corresponds well with the ADF-STEM results shown in Figure S6 b) and c).

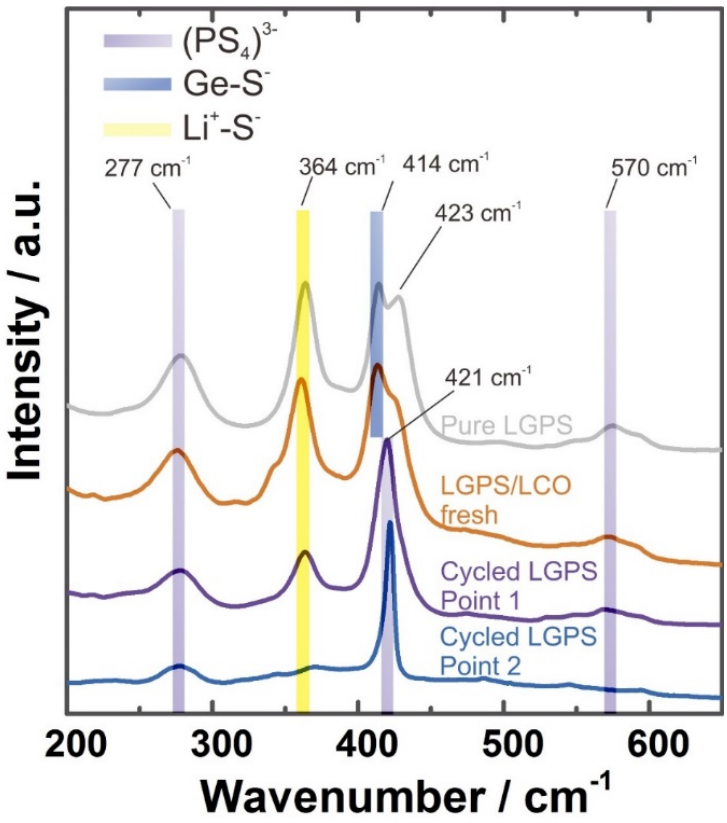

Figure S8: The comparison of cycled LGPS (two spectra were taken at different points) to freshly mixed LGPS/$LiCoO_2$ and pure LGPS using Raman spectroscopy.

In Figure S8, results of Raman spectroscopy are shown. There are no obvious differences between pure LGPS and LGPS/$LiCoO_2$ mixture.We note that the LGPS synthesized in this work shows two separate lines at 414 cm^{-1} and 423 cm^{-1}, while only a broad peak is reported in literature.[5] The better resolved lines probably indicate a higher crystallinity as well as purity of the LGPS synthesized in the work. By comparing with literature,[6] the stretching vibration of the P-S bond in the $(PS_4)^{3-}$ as the main component in LGPS structure could be assigned to the lines at 277 cm^{-1}, 423 cm^{-1} and 570 cm^{-1}.[5] In Li_3PS_4, the typical P-S stretching bond is found at 420 cm^{-1}.[7] The slight shift to 423 cm^{-1} in LGPS might be due to the participation of Ge, because Ge and P share the same Wyckoff position in the LGPS structure. The line at 414 cm^{-1} represents the Ge-S stretching bond.[8] A strong line at 361 cm^{-1} could be assigned to the Li-S stretching mode.[6,9] Comparing to the spectrum of fresh LGPS, the most obvious change in the cycled LGPS spectra lies in the 420 cm^{-1} region, where only one sharp line could be seen. The disappearance of the Ge-S- vibration mode indicates that the local structure around Ge has

changed. Compared to point 1, the spectrum at point 2 in the same composite shows only the $(PS_4)^{3-}$ at 421 cm^{-1}. The disappearance of Li-S stretching mode indicates the involvement of Li-S redox during charge process, forming a lithium depletion layer.

The variation of the recorded spectra from point to point demonstrates an inhomogeneous current distribution in the composite cathode during cycling, which leads to the decomposition of solid electrolyte to different extent. This corresponds well with the literature,[10] where distribution of reactions in the composite electrode were found through Raman mapping. The variation in degradation is further indicative of different electrochemical environments as well as various local strain effects the particles experienced. The change of current/potential distribution with the increase in cycle number may happen due to two effect: (i) The anisotropic volumetric expansion of $LiCoO_2$ during cycling (e.g. during delithiation, $Li_{1-x}CoO_2$ experiences a *c*-axis volumetric expansion of 2.6% up to x=0.5, with minor variation of *a*-axis)[11] may lead to the loss of local grain-to-grain connectivity, once the surrounding SE cannot follow the aniosotropic 'chemo-elastic' response of $LiCoO_2$ particles.[12] (ii). The decomposed products at the cathode/SE interface could in return break the balanced percolation, resulting in partially overcharged $LiCoO_2$, and/or partially more decomposed LGPS.

The most direct deleterious consequence of unbalanced ionic percolation paths is the overcharge of $LiCoO_2$ particles. As is known, once the delithiation of $Li_{1-x}CoO_2$ exceeds x = 0.5, irreversible mechanical failure associated with a large change along the *c*-axis would result in quick capacity fading.[13] Therefore, the varying electrochemical reactions of $LiCoO_2$ particles with increasing cycles can result in structural degradation with locally overcharged particles. This is further supported by the observation of the distribution of delithiation reported by Tatsumisago et al, by means of Raman image.[10]

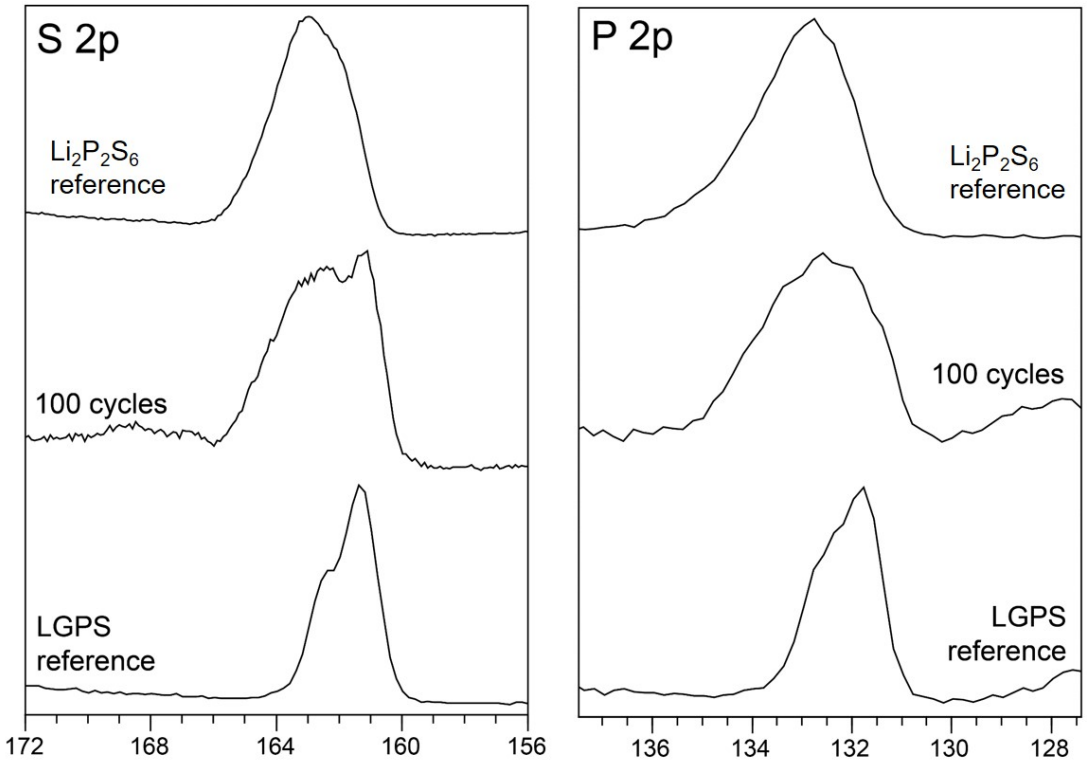

Figure S9: XPS spectra of pure $Li_2P_2S_6$ (left: S 2p. right: P 2p). The spectra of LGPS (100 cycles) and non-cycled pure LGPS are used for comparison. Comparing to pure LGPS, the spectrum of $Li_2P_2S_6$ is broader at higher binding energy. In the S 2p spectra, the main S 2p lines of $Li_2P_2S_6$ overlap well with the decomposed LGPS spectrum (namely area A and B, as shown in Figure 7). So does the P 2p spectrum (namely area C, as shown in Figure 7).

SE decomposition controlled by cell voltage: A full cell test. A full cell LTO/LGPS/c-$LiCoO_2$ was assembled and galvanostatically cycled, and the charge-discharge curves of the full cell are shown in Figure S10a. Compared to the impedance spectrum with an In anode (Figure S10b), only one major semicircle in the MF range was observed, corresponding well to the c-$LiCoO_2$/LGPS interfacial resistance. A reasonable fitting could be obtained with a *R(RQ)(RQ)Q* model, where the second *(RQ)* component may be attributed to the interface between LTO and LGPS. Interestingly, with increasing cycles, the semicircle in the MF region increases in size, while the second resistance remains constant. Thus, the increase can be largely attributed to the cathode/SE interface.

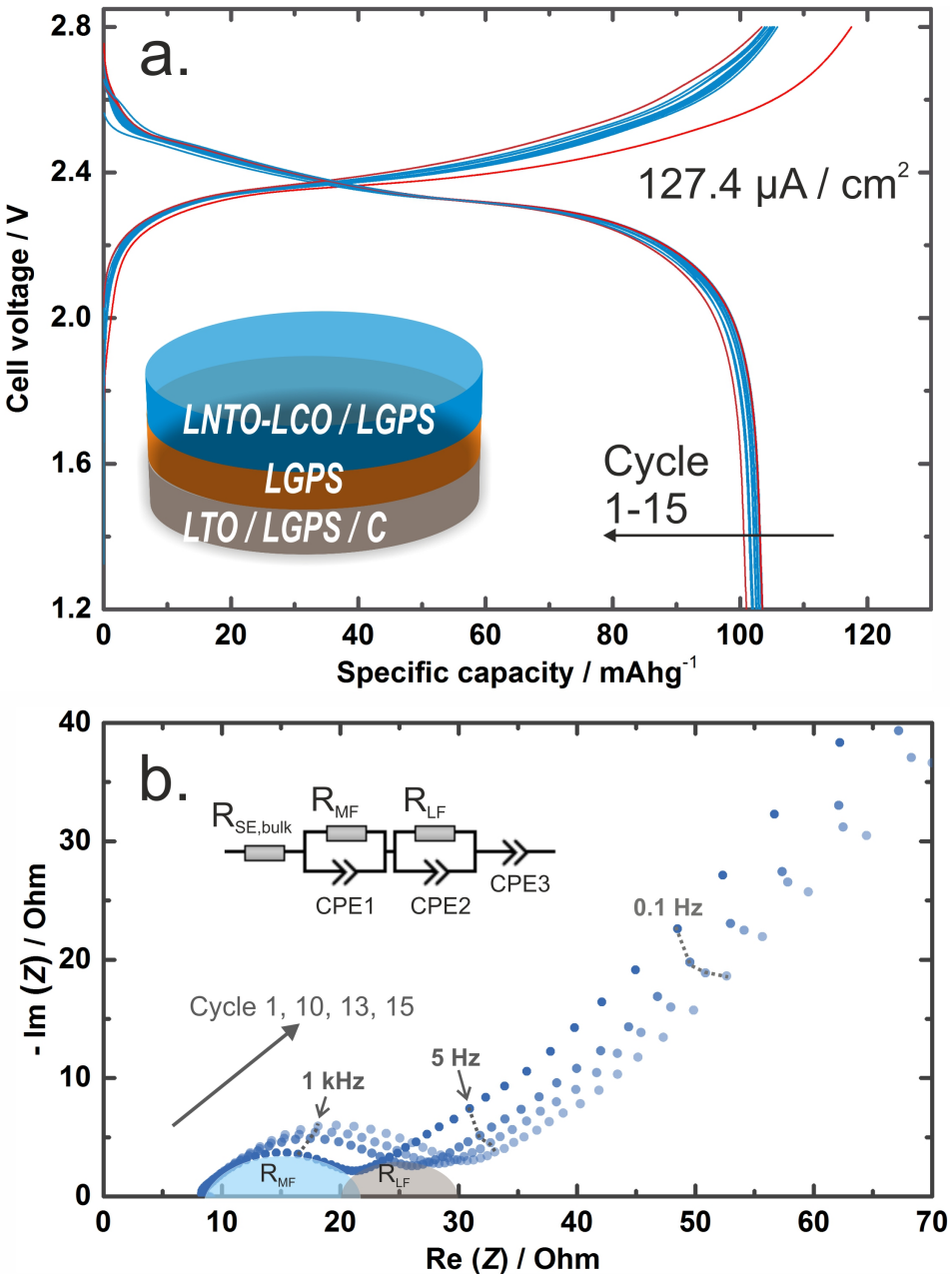

Figure S10: a) Charge-discharge curves of a LTO/LGPS/c-$LiCoO_2$ SSB full cell. b) Nyquist plot recorded after the 1st, 10th, 13th and 15th cycle. The internal resistance increases with increasing cycle number. Fitting with the R(RQ)(RQ)Q model reveals that R_{MF} increases, while R_{LF} remains unchanged with increasing cycles.

Table S1: Resistance and capacitance data used for the fitting of EIS spectra shown in Figure 2.

	After 1st cycle	After 100th cycle
R_{SE} (Ω)	15	14
R_{HF} (Ω)	3	201
CPE_{HF} (S $s^{-\alpha}$)	$1.2 \cdot 10^{-5}$	$1.9 \cdot 10^{-8}$
α_{HF}	0.8	0.8
C_{HF} (F)	$9.3 \cdot 10^{-7}$	$8.4 \cdot 10^{-10}$
R_{MF} (Ω)	28	171
CPE_{MF} (S $s^{-\alpha}$)	$9.3 \cdot 10^{-5}$	$3.9 \cdot 10^{-5}$
α_{MF}	0.7	0.6
C_{MF} (F)	$7.3 \cdot 10^{-6}$	$1.4 \cdot 10^{-6}$
R_{LF} (Ω)	14	118
CPE_{LF} (S $s^{-\alpha}$)	$1.3 \cdot 10^{-2}$	$2.9 \cdot 10^{-3}$
α_{LF}	0.8	0.6
C_{LF} (F)	$7.5 \cdot 10^{-3}$	$1.3 \cdot 10^{-3}$

Table S2: Resistance and capacitance data used for the fitting of EIS spectra shown in Figure 8.

	1st	10th	13rd	15th
R_{SE} (Ω)	8	8	8	8
R_1 (Ω)	13	18	20	22
CPE_1 (S $s^{-\alpha}$)	$2.5 \cdot 10^{-4}$	$2.5 \cdot 10^{-4}$	$2.2 \cdot 10^{-4}$	$2.2 \cdot 10^{-4}$
α_1	0.62	0.62	0.62	0.61
C_1 (F)	$7.5 \cdot 10^{-6}$	$6.8 \cdot 10^{-6}$	$7.8 \cdot 10^{-6}$	$7.2 \cdot 10^{-6}$
R_2 (Ω)	11	10	10	10
CPE_2 (S $s^{-\alpha}$)	0.040	0.048	0.051	0.053
α_2	0.56	0.57	0.52	0.52
C_2 (F)	$2.1 \cdot 10^{-2}$	$2.7 \cdot 10^{-2}$	$2.7 \cdot 10^{-2}$	$2.9 \cdot 10^{-2}$
R_{total} (Ω)	32	36	38	40

Table S3: Fit parameters used for the post-mortem XPS analysis shown in Figure 6.

		S 2p3/2						P 2p3/2			Ge 3d		
pristine LGPS	Component	Ge/P)-S	A	B	-S-S-	SOx (1)	SOx (2)	PS4	C	D	GeS4	E	F
	Binding Energy (eV)	161.3	162.3	163.4	-	-	-	131.8	133.0		30.7	-	-
	FWHM (eV)	1.2	1.3	1.3	-	-	-	1	1		1.3	-	-
	relative Composition	97%	2%	2%		-	-	93%	7%		100%	-	-
		S 2p3/2						P 2p3/2			Ge 3d		
fresh cathode composite	Component	Ge/P)-S	A	B	-S-S-	SOx (1)	SOx (2)	PS4	C	D	GeS4	E	F
	Binding Energy (eV)	161.3	162.4	163.3	-	-	-	131.8	133.0		30.8	-	-
	FWHM (eV)	1.2	1.2	1.2	-	-	-	1	1		1.4	-	-
	relative Composition	94%	4%	2%	-	-	-	90%	10%		100%	-	-
		S 2p3/2						P 2p3/2			Ge 3d		
cathode composite after 1 cycle	Component	Ge/P)-S	A	B	-S-S-	SOx (1)	SOx (2)	PS4	C	D	GeS4	E	F
	Binding Energy (eV)	161.2	162.3	163.3	163.9	167.0	168.7	131.8	133.0		30.7	31.9	32.4
	FWHM (eV)	1.2	1.2	1.2	1.1	1.2	1.4	1.0	1.0		1.3	1.3	1.3
	relative Composition	78%	8%	8%	1%	3%	2%	78%	22%		77%	19%	5%
		S 2p3/2						P 2p3/2			Ge 3d		
cathode composite after 10 cycles	Component	Ge/P)-S	A	B	-S-S-	SOx (1)	SOx (2)	PS4	C	D	GeS4	E	F
	Binding Energy (eV)	161.2	162.2	163.2	163.9	166.8	168.7	131.8	133.4	134.5	30.7	31.5	32.4
	FWHM (eV)	1.2	1.2	1.1	1.1	1.1	1.6	1.2	1.2	1.2	1.2	1.2	1.2
	relative Composition	59%	10%	10%	7%	9%	6%	79%	20%	1%	49%	35%	16%
		S 2p3/2						P 2p3/2			Ge 3d		
cathode composite after 100 cycles	Component	Ge/P)-S	A	B	-S-S-	SOx (1)	SOx (2)	PS4	C	D	GeS4	E	F
	Binding Energy (eV)	161.1	162.2	163.2	163.9	166.8	168.7	131.9	133.2	134.3	30.7	31.5	32.4
	FWHM (eV)	1.2	1.2	1.2	1.2	1.1	1.4	1.3	1.3	1.3	1.2	1.2	1.2
	relative Composition	46%	13%	23%	10%	4%	4%	58%	38%	4%	40%	40%	19%

References

(1) Ohta, N.; Takada, K.; Zhang, L.; Ma, R.; Osada, M.; Sasaki, T. Enhancement of the High-Rate Capability of Solid-State Lithium Batteries by Nanoscale Interfacial Modification. *Adv. Mater.* **2006**, *18* (17), 2226–2229.

(2) Ohta, N.; Takada, K.; Sakaguchi, I.; Zhang, L.; Ma, R.; Fukuda, K.; Osada, M.; Sasaki, T. $LiNbO_3$-Coated $LiCoO_2$ as Cathode Material for All Solid-State Lithium Secondary Batteries. *Electrochem. commun.* **2007**, *9* (7), 1486–1490.

(3) Zhang, W.; Weber, D. A.; Weigand, H.; Arlt, T.; Manke, I.; Schröder, D.; Koerver, R.; Leichtweiss, T.; Hartmann, P.; Zeier, W. G.; et al. Interfacial Processes and Influence of Composite Cathode Microstructure Controlling the Performance of All-Solid-State Lithium Batteries. *ACS Appl. Mater. Interfaces* **2017**, *9* (21), 17835–17845.

(4) Wang, Z.; Santhanagopalan, D.; Zhang, W.; Wang, F.; Xin, H. L.; He, K.; Li, J.; Dudney, N.; Meng, Y. S. In Situ STEM-EELS Observation of Nanoscale Interfacial Phenomena in All-Solid-State Batteries. *Nano Lett.* **2016**, *16* (6), 3760–3767.

(5) Yang, K.; Dong, J.; Zhang, L.; Li, Y.; Wang, L. Dual Doping: An Effective Method to Enhance the Electrochemical Properties of $Li_{10}GeP_2S_{12}$ -Based Solid Electrolytes. *J. Am. Ceram. Soc.* **2015**, *98* (12), 3831–3835.

(6) Hassoun, J.; Verrelli, R.; Reale, P.; Panero, S.; Mariotto, G.; Greenbaum, S.; Scrosati, B. A Structural, Spectroscopic and Electrochemical Study of a Lithium Ion Conducting $Li_{10}GeP_2S_{12}$

Solid Electrolyte. *J. Power Sources* **2013**, *229*, 117–122.

(7) Busche, M. R.; Weber, D. A.; Schneider, Y.; Dietrich, C.; Wenzel, S.; Leichtweiss, T.; Schröder, D.; Zhang, W.; Weigand, H.; Walter, D.; et al. In Situ Monitoring of Fast Li-Ion Conductor $Li_7P_3S_{11}$ Crystallization Inside a Hot-Press Setup. *Chem. Mater.* **2016**, *28* (17), 6152–6165.

(8) Kim, Y.; Saienga, J.; Martin, S. W. Glass Formation in and Structural Investigation of Li_2S-GeS_2-GeO_2 Composition Using Raman and IR Spectroscopy. *J. Non. Cryst. Solids* **2005**, *351* (49–51), 3716–3724.

(9) Sang, L.; Haasch, R. T.; Gewirth, A. A.; Nuzzo, R. G. Evolution at the Solid Electrolyte/Gold Electrode Interface during Lithium Deposition and Stripping. *Chem. Mater.* **2017**, *29*, 3029–3037.

(10) Otoyama, M.; Ito, Y.; Hayashi, A.; Tatsumisago, M. Raman Imaging for $LiCoO_2$ Composite Positive Electrodes in All-Solid-State Lithium Batteries Using Li_2S-P_2S_5 Solid Electrolytes. *J. Power Sources* **2016**, *302*, 419–425.

(11) Reimers, J.; Dahn, J. Electrochemical and In Situ X-Ray Diffraction Studies of Lithium Intercalation in Li_xCoO_2. *J. Electrochem. Soc.* **1992**, *139* (8), 2091–2097.

(12) Malave, V.; Berger, J. R.; Kee, R. J. The Influence of Crystallographic Orientation on the Chemo-Elastic Response of Reconstructed Li_xCoO_2 Cathode Particles. *J. Electrochem. Soc.* **2014**, *161* (11), F3156–F3163.

(13) Ohzuku, T. 47. Solid-State Redox Reactions of $LiCoO_2$ (R3m) for 4 Volt Secondary Lithium Cells. *J. Electrochem. Soc.* **1994**, *141* (11), 2972.